AD

AD-E403 106

Technical Report ARAET-TR-07001

ENGINEERING MODEL FOR DESIGN OF EXPLOSIVE FRAGMENTATION MUNITIONS

Vladimir M. Gold

February 2007

ARMAMENT RESEARCH, DEVELOPMENT AND ENGINEERING CENTER

Armaments Engineering & Technology Center

Picatinny Arsenal, New Jersey

The views, opinions, and/or findings contained in this report are those of the author(s) and should not be construed as an official Department of the Army position, policy, or decision, unless so designated by other documentation.

The citation in this report of the names of commercial firms or commercially available products or services does not constitute official endorsement by or approval of the U.S. Government.

Destroy this report when no longer needed by any method that will prevent disclosure of its contents or reconstruction of the document. Do not return to the originator.

REPORT DOCUMENTATION PAGE	*Form Approved OMB No. 0704-01-0188*

1. REPORT DATE (DD-MM-YYYY)	2. REPORT TYPE	3. DATES COVERED (*From - To*)
February 2007		

4. TITLE AND SUBTITLE	5a. CONTRACT NUMBER
ENGINEERING MODEL FOR DESIGN OF EXPLOSIVE FRAGMENTATION MUNITIONS	5b. GRANT NUMBER
	5c. PROGRAM ELEMENT NUMBER
6. AUTHORS	5d. PROJECT NUMBER
Vladimir M. Gold	5e. TASK NUMBER
	5f. WORK UNIT NUMBER

7. PERFORMING ORGANIZATION NAME(S) AND ADDRESS(ES)	8. PERFORMING ORGANIZATION REPORT NUMBER
U.S. Army ARDEC, AETC Energetics and Warheads (AMSRD-AAR-AEE) Picatinny Arsenal, NJ 07806-5000	
9. SPONSORING/MONITORING AGENCY NAME(S) AND ADDRESS(ES)	10. SPONSOR/MONITOR'S ACRONYM(S)
U.S. Army ARDEC, EM Technical Research Center (AMSRD-AAR-EMK) Picatinny Arsenal, NJ 07806-5000	11. SPONSOR/MONITOR'S REPORT NUMBER(S) Technical Report ARAET-TR-07001

12. DISTRIBUTION/AVAILABILITY STATEMENT

Approved for public release; distribution is unlimited.

13. SUPPLEMENTARY NOTES

14. ABSTRACT

An engineering model for design of explosive fragmentation munitions presented in this work is based on integrating three-dimensional axisymmetric hydrocode analyses with analyses from a newly developed fragmentation computer code MOTT. The validation of the MOTT code fragmentation model was accomplished using the existing munition arena test data. After having established the crucial parameters of the model, a new explosive fragmentation munitions was designed and optimized. Upon fabrication of the developed munition, the performance of the new charge was tested in a series of small-scale experiments including the flash radiography, the high-speed photography, and the sawdust fragment recovery. Considering relative simplicity of the model, the accuracy of the MOTT code predictions is rather remarkable.

15. SUBJECT TERMS

Fragmentation	Fragmentation modeling	Natural fragmentation	Fragmentation warhead
Airburst warhead	M789	ALACV	MOTT theory

16. SECURITY CLASSIFICATION OF:			17. LIMITATION OF ABSTRACT	18. NUMBER OF PAGES	19a. NAME OF RESPONSIBE PERSON
a. REPORT	b. ABSTRACT	c. THIS PAGE			Dr. Vladimir Gold
U	U	U	SAR	23	19b. TELEPHONE NUMBER (Include area code) (973) 724-5977

ACKNOWLEDGMENTS

The germinal concept of integrating the CALE hydrocode analyses and analytical fragmentation modeling WAS due to Dr. E. L. Baker of the U.S. Army Armament Research, Development and Engineering Center (ARDEC), Picatinny Arsenal, New Jersey. K. W. Ng of ARDEC is acknowledged for his contributions in preparing the CALE model employed in these analyses. W. J. Poulos and Dr. B. E. Fuchs both of ARDEC are acknowledged for obtaining the experimental data presented in this work. The work was conducted under the auspices of the ALACV Warhead Program. Dr. E. L. Baker and J. M. Hirlinger of ARDEC are acknowledged for making this work possible.

CONTENTS

FIGURES

INTRODUCTION

A technique for predicting performance of explosive fragmentation munitions presented in this work is based on integrating the CALE computer program (ref. 1) with a newly developed fragmentation computer code MOTT. CALE is a two-dimensional and three-dimensional axial symmetric high rate finite difference computer program based on Arbitrary Lagrangian-Eulerian formulation of the governing equations. The mathematical description of the MOTT code is given in a section that follows.

The geometries of two example problems are shown in figure 1. Upon initiation of the high explosive charges, rapid expansion of high-pressure high-velocity detonation products results in high-strain high-strain-rate dilation of the hardened steel shells, which eventually rupture generating a "spray" of high-velocity steel fragments. In the case of the ***Charge A***, the dilation of the steel shell is accompanied by the implosion of the copper shaped charge liner that produces a high-speed metal jet moving along the charge's axis of symmetry *z*. In the case of the ***Charge B***, in addition to the explosive charge, the hardened steel shell also encapsulates a tracer and a fuze that occupy significant volume of the munition payload. A threaded connection between the fuse and the fragmenting portion of the hardened steel case was also included into the CALE model. In order to allow slippage, the threaded joint was modeled with a few rows of computation cells employing ideally-plastic-zero-yield-strength material with the same hydrodynamic response parameters as steel. Following the expansion of the detonation products, the fuze section of the warhead is projected in the negative direction of the *z*-axis, without contributing to the lethality of the fragment spray.

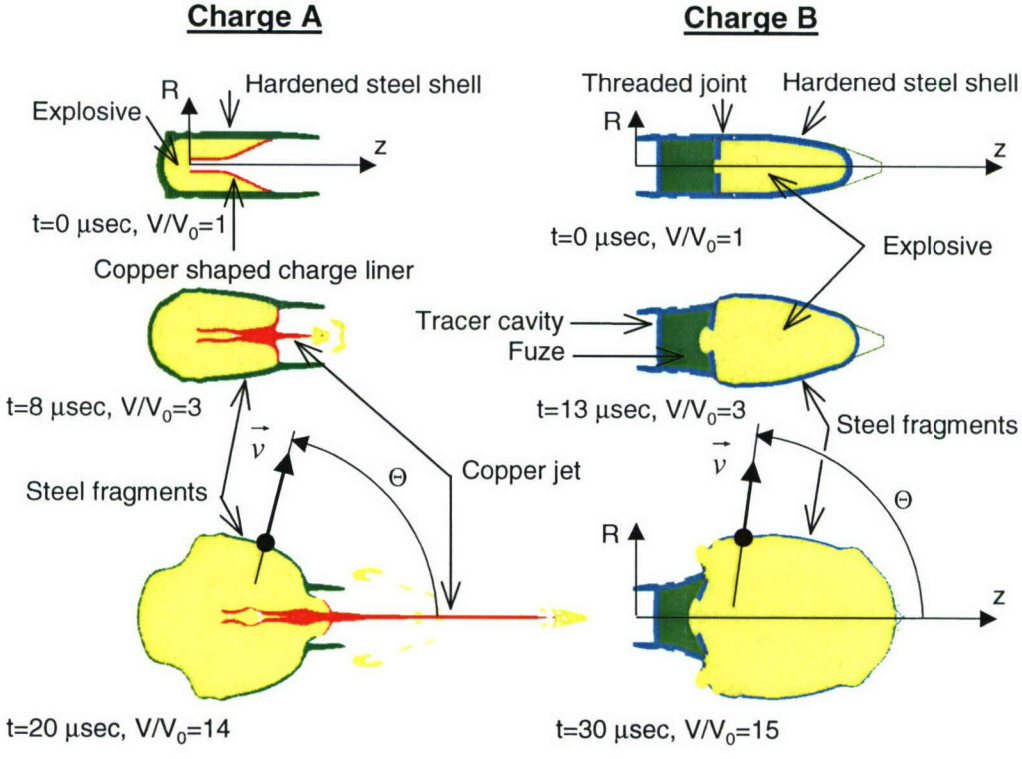

Figure 1
Results of CALE-code modeling: initial configuration and CALE's predictions following the explosive detonation initiation

In addition to the specification of the problem geometry and initial and boundary conditions, equations of states and constitutive equations for all materials have to be specified before the solution procedure can be initiated. The explosive was modeled using the Jones-Wilkins-Lee-Baker equation of state employing a set of parameters resulting from thermo-chemical equilibrium analyses of detonation products with the JAGUAR code and calibrated with copper cylinder test expansion data. The hydrodynamic responses of the steel shell and the copper liner were modeled using a standard linear polynomial approximation usually employed for metals. The constitutive behavior of these metals was modeled using the Steinberg-Guinan yield-strength model and the von Mises yielding criterion. A standard set of parameters available from Tipton (ref. 2) were employed in the analyses.

Since the extent of dilation of the rapidly expanding steel shell is limited by its strength, at some point the shell ruptures generating a spray of steel fragments moving with trajectories at angles Θ with *z*-axis. Accordingly, the principal topic of this work is a numerical model for the analytical description of parameters of the resulting fragment spray as functions of the "spray" angle Θ. In typical large-scale explosive fragmentation tests (arena tests), the tested munitions are positioned at the origin of the reference polar coordinate system and surrounded with series of velocity-measuring screens and fragment-catching witness panels, all at significant distances from the warhead. Accordingly, the fragmentation characteristics are assessed as functions of polar angles Θ' identifying angular positions of these measuring devices. Assuming that the fragment trajectory angles Θ do not change with time (that is the lateral drift of fragments due to air resistance is small) and that definitions of angles Θ and Θ' are approximately identical, the developed model enables prediction of crucial characteristics of explosive fragmenting munitions including the number of fragments, the fragment size distribution, and the average fragment velocities.

MOTT CODE FRAGMENTATION MODEL

For a large part, the MOTT code fragmentation model is based on the Mott's theory of break-up of cylindrical "ring-bombs" (ref. 3), in which the average length of the resulting circumferential fragments is a function of the radius and velocity of the ring at the moment of break-up, and the mechanical properties of the metal. A brief review of the Mott's theory is given here for completion. Following Mott and Linfoot (ref. 4), the "random variations" in fragment sizes are accounted through the following fragment distribution relationship

$$N(m) = N_0 e^{-\left(m/\mu\right)^{1/2}} \tag{1}$$

In equation 1, $N(m)$ represents total number of fragments of mass greater than m ; μ is defined as one half of the average fragment mass, $N_0 = M/\mu$ and M is the total mass of the fragments.

In attempting to evaluate the distribution of fragment sizes occurring in the dynamic fragmentation of expanding metal rings, Mott (ref. 3) introduced an idealized model in which the average circumferential fragment lengths are not random, but determined by the interaction of stress release waves originating from instantaneous fractures in the body. A schematic of the Mott's model is shown in figure 2 (a). Assuming that a fracture in the ring is supposed to have

occurred first at A_1 and that stress release waves have traveled to points B_1 and $\underline{B}_1$, further fractures can no longer take place in regions A_1B_1 and $\underline{A}_1\underline{B}_1$. On the other hand, in the regions B_1B_2 and $\underline{B}_1\underline{B}_2$ the plastic strain is increasing, which increases the probability of fractures at any point in these regions, especially at points B_1, B_2, $\underline{B}_1$, and $\underline{B}_2$. Thus, according to Mott's theory, the average size of fragments is determined by the rate at which stress relieved regions A_1B_1 and $\underline{A}_1\underline{B}_1$ spread through the plastically expanding ring.

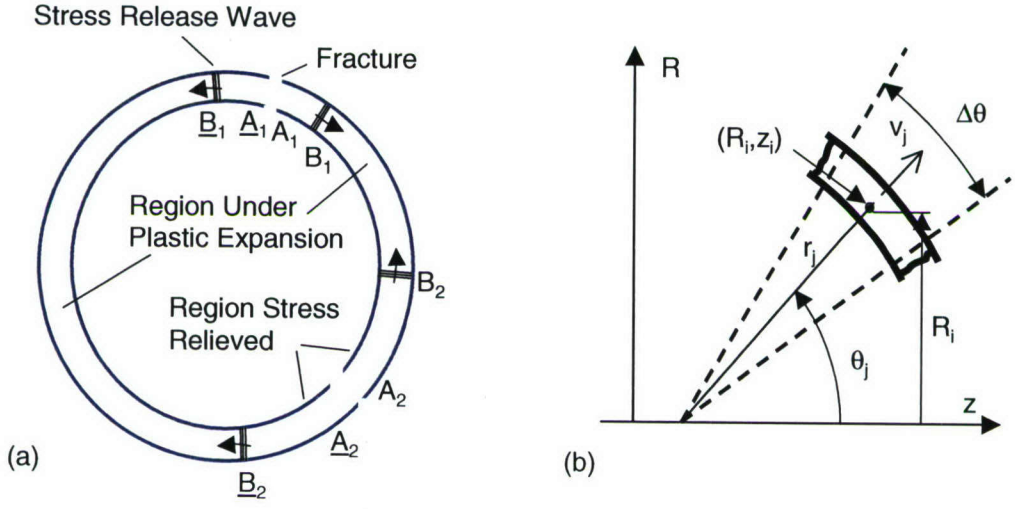

Figure 2
Fragmentation model

At the moment of fracture, let r be the radius of the ring and V be the velocity with which the shell is moving outwards. Then, according to Mott (ref. 3), the average circumferential length of the resulting fragments is

$$x_0 = \left(\frac{2P_F}{\rho\gamma}\right)^{1/2} \frac{r}{V} \tag{2}$$

In equation 2, ρ and P_F denote the density and the strength, respectively; and γ is a semi-empirical statistical constant determining the dynamic fracture properties of the material. Given that the shape and the average fragment lengths are known, the idealized average fragment mass can be calculated. For example, assuming approximate cubic-shaped fragments, μ takes the following form

$$\mu = \frac{1}{2}\rho x_0^3 \tag{3}$$

A schematic for the newly developed technique implemented in the MOTT code is shown in figure 2 (b). For computational purposes, the shell is discretized into a finite number of short "ring" segments, N. For each discrete ring element, j uniform field variables are assumed. Accordingly, the masses, the velocities, and radii of ring segments j are defined by the mass averages of the respective parameters

$$m_j = \sum_{L_j} m_i \tag{4}$$

$$v_j = \frac{\sum_{L_j} v_i m_i}{m_j} \tag{5}$$

$$r_j = \frac{\sum_{L_j} R_i m_i}{m_j} \cdot \frac{1}{\sin\Theta_j} \tag{6}$$

$$\Theta_j - \frac{\pi}{2N} \le \Theta_i < \Theta_j + \frac{\pi}{2N} \tag{7}$$

In equations 4 through 6 m_i, v_i, and R_i denote the mass, the velocity, and the radial coordinate of the *i-th* computational cell from the CALE-code generated data. L_j denotes a number of computational cells contained in the *j-th* ring segment. Θ_j denotes the Θ-angle that corresponds to the *j-th* ring segment given by

$$\Theta_j = \frac{\pi}{2N} \cdot \left(j - \frac{1}{2} \right) \tag{8}$$

For each computational cell i, the velocity v_i and the Θ angle, Θ_i, are calculated, respectively, by

$$v_i = \sqrt{v_{zi}^2 + v_{Ri}^2} \tag{9}$$

and

$$\Theta_i = \arctan \frac{v_{Ri}}{v_{zi}} \tag{10}$$

In equations 9 and 10, v_{zi} and v_{Ri} denote the axial and the radial velocity components from the CALE-code generated data.

Given that the velocities and the radii of ring segments j are determined through equations 5 and 6, the resulting fragment size distributions in each segment j can be calculated through the following relationships

$$N_j(m) = N_{0j} e^{-\left(m/\mu_j\right)^{1/2}} \tag{11}$$

$$\mu_j = \sqrt{\frac{2}{\rho}} \left(\frac{P_F}{\gamma} \right)^{3/2} \left(\frac{r_j}{V_j} \right)^3 \tag{12}$$

$$N_{0j} = \frac{m_j}{\mu_j} \tag{13}$$

As the detonation wave travels along the shell length and the expanding detonation products rupture the shell, in the case of the idealized "long-pipe-bombs," the break-up radii r_j and the break-up velocities V_j of the individual segments j are approximately the same, regardless of the axial positions of the segments. Accordingly, taking $\mu \approx \mu_j$, the number of fragment distribution relationship is given by the original Mott's equation 1.

However, in the case of conventional explosive fragmentation munitions with shell geometries far from that of the idealized "long-pipe-bombs," the break-up radii r_j and the break-up velocities V_j vary along the shell length, so that the resulting variance in the average fragment half-weights μ_j of the individual segments j may be rather significant. The existence of significant differences in the average fragment sizes between the cylindrical and the curved portions of the shell had been experimentally confirmed in this work through flash radiography and high-speed photography. Accordingly, the following two fragment distribution relationships are introduced herein. The "shell-averaged" fragment distribution is defined as

$$N(m) = \tilde{N}_0 e^{-\left(m/\tilde{\mu}_0\right)^{1/2}} \tag{14}$$

where $\tilde{N}_0$ and $\tilde{\mu}_0$ are defined as

$$\tilde{N}_0 = \sum_j N_{0j} \tag{15}$$

$$\tilde{\mu}_0 = \frac{\sum_j m_j}{2\tilde{N}_0} \tag{16}$$

The "ring-segment-averaged" fragment distribution is defined as

$$N(m) = \sum_j N_{0j} e^{-\left(m/\mu_j\right)^{1/2}} \tag{17}$$

MOTT CODE VALIDATION: CHARGE A ANALYSES

The validation of the MOTT code fragmentation model was accomplished using the existing ***Charge A*** arena test data. The fundamental assumption of all fragmentation analyses presented in this work was that the fragmentation occurs instantly throughout the entire body of the shell. Following Mott's critical fracture strain concept (ref. 3) and assuming that for given shell geometry and materials, the shell fragmentation time is a function of the cumulative dilatational plastic strain in the shell, the shell fragmentation time can be conveniently

expressed in terms of the global shell dilatational properties. Given that in a typical fragmentation munition device the explosive is tightly confined inside the shell, the cumulative strains of the expanding explosive and the surrounding shell are nearly proportional. Accordingly, the critical fracture strain at the moment of the shell break-up may be conveniently measured in terms of the high explosive detonation products volume expansions, V/V_0.

Figure 3 shows the effect of the shell fragmentation time on the fragment spray velocity distribution function. The seemingly significant disagreement between the experimental velocities and the analyses for $\Theta \leq 15°$ is due to deliberate omission of the shaped charge jet data from the MOTT fragmentation analyses, mainly because of the minimal contribution to the overall fragment-spray lethality. Accordingly, the copper shaped charge jet was neglected in all fragmentation analyses, although included in the CALE model in order to maintain proper explosive confinement parameters. As shown in figure 3, varying the shell fragmentation time from approximately 8 μs (at which the detonation products had expanded approximately three times its original volume, $V/V_0 \sim 3$ to approximately 20 μs ($V/V_0 \sim 14$), the resulting changes in the fragment spray angles Θ were rather small, while the fragment spray velocities were affected rather significantly. As shown in figure 3, delaying the moment of the shell break-up predicts considerable increases in the fragment spray velocities, apparently due to the prolonged "pressurized" interaction with expanding detonation products that increased the total momentum transferred to the shell.

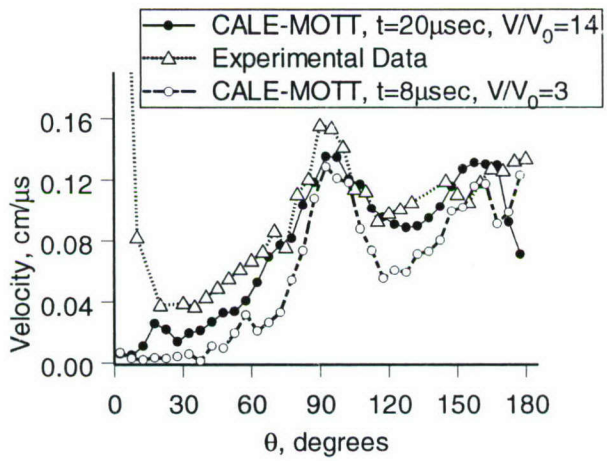

Figure 3
Fragment velocity distribution versus spray angle Θ change A

Figures 4 through 6 show plots of the number of fragments in the fragment spray as functions of the fragment size m/μ, the choice of the number of fragment distribution function model, equations 14 and 17, the spray angle Θ, the shell fragmentation time, and the dynamic fracture parameter γ. As shown in the figures, increases in the parameter γ had resulted in increases of the number of fragments N, both for the $N-m/\mu$ and the $N-\Theta$ relationships. These results are in agreement with the Mott's theory (ref. 3), according to which the parameter γ defines the probability of fracture in the plastically expanding shell determining the number of breaks in the circumferential direction.

Figure 4 shows a plot of a series of curves given by equation 14, $N(m)=f_{(14)}(m,\gamma)$, all analyses repeated for two parameters considered: the shell fragmentation time assumed and the dynamic fracture constant, γ. For example, taking the 8 μs (V/V_0 ~3.0) fragmentation time with γ=12 and the 20 μs (V/V_0 ~14) fragmentation time with γ=30 resulted in nearly identical fragment distribution curves, both in good agreement with the data. The accepted shell fragmentation time was determined from the high-speed photographic data of Pearson (ref. 5). Following Pearson (ref. 5), the fragmentation of shells with the idealized cylindrical geometries occurs approximately at 3 volume expansions, the instant of fragmentation defined as the time at which the detonation products first appear emanating from the fractures in the shell. Accordingly, the accepted shell fragmentation time was approximately 8 μs (V/V_0 ~3.0).

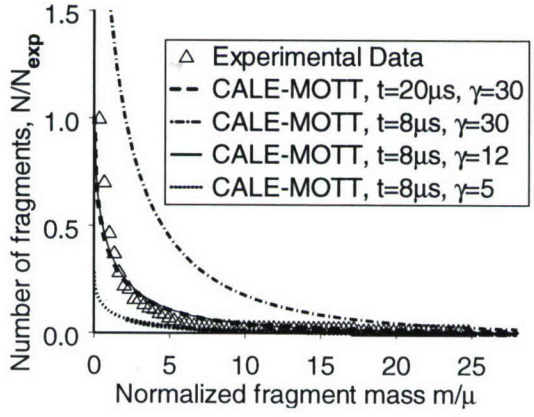

Figure 4
Cumulative number of fragments in the fragment spray versus the fragment size m/μ charge A

Figure 5 shows a plot of the cumulative number of fragments from the arena test data and the CALE-MOTT analytic predictions employing $N(m)=f_{(14)}(m,\gamma)$ and $N(m)=f_{(17)}(m,\gamma)$ relationships; i.e., the overall "shell-averaged" fragment size distribution, equation 14, and the "ring-segment-averaged" fragment size distribution, equation 17, respectively. As shown in the plot, employing equation 14 resulted in consistently higher values of the cumulative numbers of fragments than that of equation 17, apparently because of the nature of the definition of the overall "shell-average" fragment mass $\tilde{\mu}_0$, equation 16. As shown in the figure, two equally reasonable fits were obtained for both relationships considered, resulting in γ=12 for equation 14 and in γ=14 for equation 17 with the standard deviations of approximately $\sigma\gamma=_{12}(1.62)=2\%$ and $\sigma\gamma=_{14}(1.62)=2\%$, respectively. Both curves were fitted at a single point $m/\mu=1.62$, which corresponds to the total number of fragments with mass greater than 3 grains; the aim was to replicate the overall lethality of the fragmenting spray, rather than focusing on the entire range of the m/μ values considered. Accordingly, the accepted shell fragmentation had been approximately 8 μs (V/V_0 ~3.0) and two values γ=12 and γ=14 were selected for all further analyses.

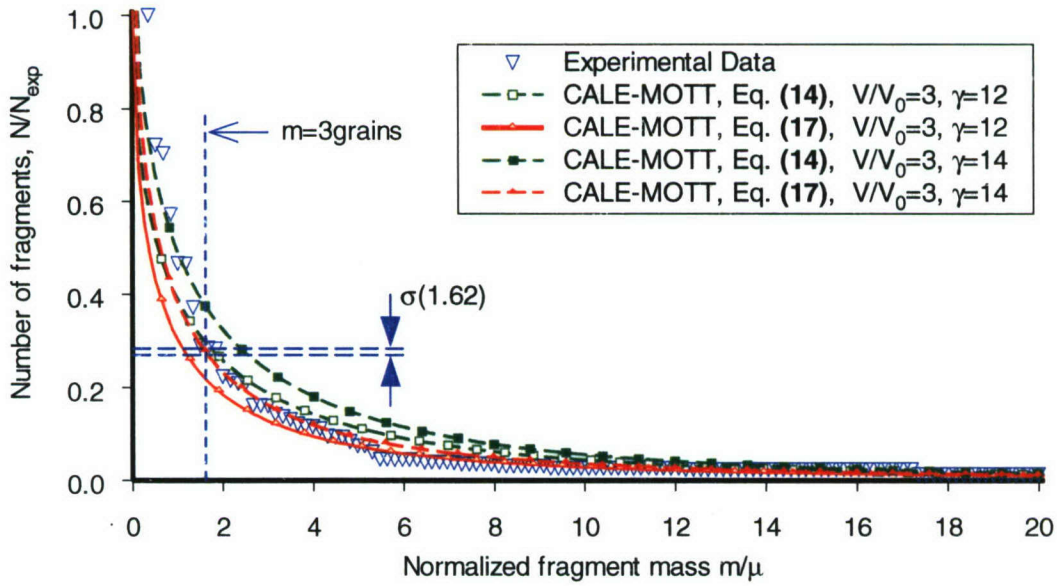

Figure 5
Cumulative number of fragments versus m/μ for varying γ CALE-MOTT analyses using equations 14 and 17 - change A

Figure 6 shows a plot of the number of fragments with mass greater than 3 grains versus the spray angle Θ, which is the principal lethality parameter of the fragment spray of the munition. The disagreement between the analyses and small spikes at 45 and 60 deg is due to fragments from the shaped charge liner-retaining ring, which had not been included in the CALE model, mainly because of the minimal effect on the overall fragment lethality. The disagreement between the analyses and the spike at 155 deg is due to fragments from a rotating band that had not been included in the CALE model. As shown in the figure, even using a relatively crude assumption of the shell fragmentation time, the overall agreement between the analyses and the experimental data is very good.

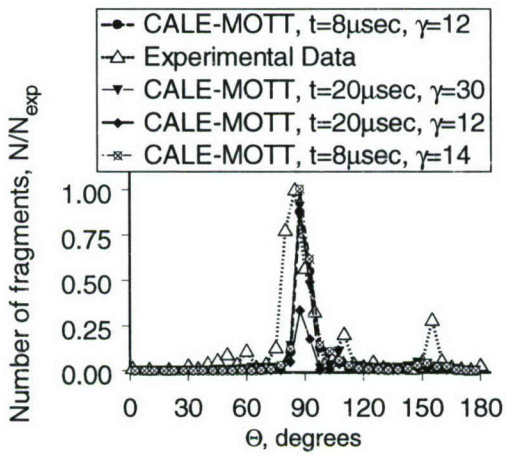

Figure 6
Number of fragments in the spray: varying the shell fragmentation time and the γ - charge A

CHARGE B MODELING AND EXPERIMENTATION

After having established the crucial parameters of the model, ***Charge B*** shown in figure 1 was designed and optimized. Upon fabrication, the performance of the new charge was tested in a series of experiments including flash radiography, high-speed photography, and sawdust fragment recovery.

The flash radiography tests were performed using two 150 kV x-ray heads located approximately 74 in. in front of the round. Shortly after initiating the round, each of the two x-rays heads were flashed at the separate prescribed times and intervals several microseconds apart. Two flash radiography tests were conducted. Each test resulted in two dynamic images of the expanding fragmented steel shell, both images superimposed on the film.

The high-speed photography tests were performed employing a Cordin Framing Camera, Model No. 121, capable of recording up to 26 high-speed exposure frames with time intervals between individual frames of less than 1 μs apart. In the experiments, the round was placed on a test stand in front of a fiducial grid, surrounded with four Argon gas light bombs, all enclosed in a white paper tent. A total of two high-speed photography tests were conducted, each test resulting in over 20 dynamic images of the expanding and fragmenting shell, approximately 1 μs apart.

Figure 7 shows a comparison between the CALE code predictions and the images of the expanding and partially fractured shell obtained from the flash radiography and high-speed photography experiments. The figure shows that the model resulted in an accurate prediction of the shape of the expanding hardened steel shell, including the early break out of the detonation products through the joint between the fuze and the main charge.

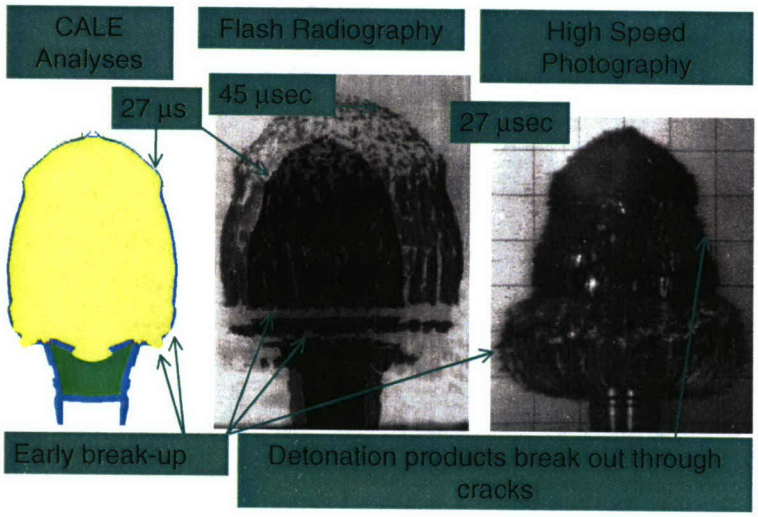

Figure 7
CALE code modeling and experimentation - charge B

Referring to the flash radiographic image of the partially fragmented shell given in figure 7, it is important to note a remarkable difference between shapes and sizes of fragments ejected from the cylindrical and the curved portions of the charge. As seen from both the 27 μs and from the 45 μs radiographic images, the majority of cracks in the cylindrical portion of the charge are in the axial direction, resulting in a fragment spray with relatively large axially oriented splinter-like fragments. On the contrary, in the curved nose portion of the shell, the orientation of cracks is random and the distances between fissures are shorter, resulting in a fragment spray of predominantly small compactly shaped fragments.

Figure 8 shows a series of high-speed photographic images of the condition of the surface as the hardened steel shell expands and the detonation products emerge through the cracks. As shown in the figure, visible fractures start to appear on the surface of the shell at approximately 9.4 μs after the detonation, which according to the CALE code analyses corresponds to approximately V/V_0=1.8. Examination of the entire series of images taken approximately 1 μs apart shows that as the shell expands, fractures develop first in the cylindrical portion of the shell. As the shell continues to expand, the developed fractures propagate mostly in the axial direction, occasionally linking-up by new cross-cracks in the circumferential direction, ultimately resulting in formation of large splinter-like fragments shown in the radiographic images of figure 7.

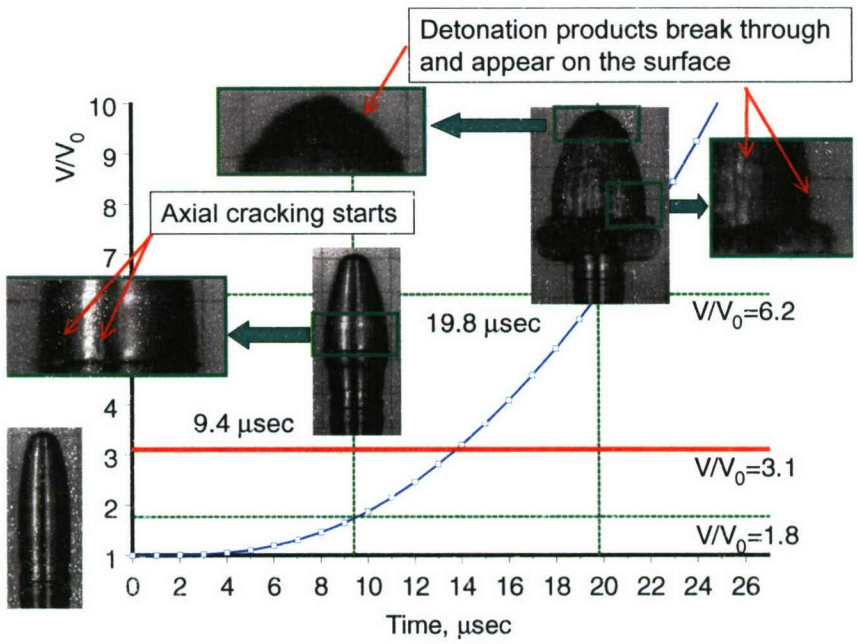

Development of surface fractures in the expending shell - charge B

As the shell continues to expand, fractures gradually advance towards the curved nosed portion of the shell, and at approximately 19.8 μs, or at approximately 6.2 volume expansions, the entire shell is fully fragmented, the fragmentation being defined as the instant at which the detonation products first appear as they emanate from the fractures in the shell. Following the

CALE-MOTT model assumption that the critical fracture strain at the moment of the shell break-up is expressed in terms of the high explosive detonation products volume expansions, the "average" volume expansion at the time of the shell break-up is then approximately one-half of the value of volume expansions of the fully fragmented shell, hence V/V_0=3.1. It is interesting to note that the value of V/V_0=3.1 is in excellent agreement with that assumed initially based on the high-speed photographic data of Pearson (ref. 5).

Figure 9 shows plots of CALE-MOTT analytic predictions of the fragment velocity distribution function and the experimental data. The experimental data considered here was reduced from the radiographic images of the expanding and partially fractured shell. As shown in the figure, two analytical fragment velocity distribution functions were considered: (i) assuming that the entire shell fragments instantly at approximately at 13 μs (V/V_0=3), and (ii) assuming that the entire shell fragments instantly at approximately at 30 μs (V/V_0=15). Given that the explosive was modeled using a semi-empirical set of parameters calibrated with the experimental copper cylinder expansion data, the CALE predictions of the expanding (but not fractured) shell velocities should be reasonably accurate. As shown in the figure, the agreement between the data and the V/V_0=3 curve is significantly better than with the V/V_0=15 curve, suggesting that the shell fractured at approximately 3 volume expansions. In addition, given that (according to the high-speed photography) the entire shell had fully fractured at approximately 6.2 volume expansions, the assumption of the V/V_0=3 instantaneous fracture event is quite reasonable: once the detonation products start to escape through the cracks, any further gains in the velocities are relatively small and may be neglected.

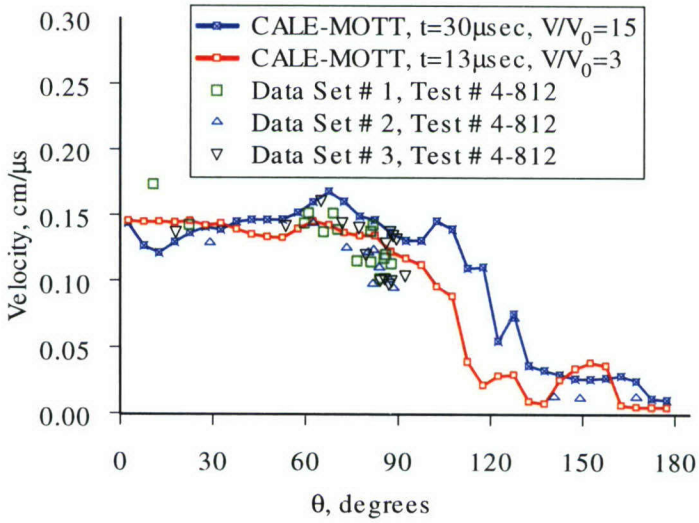

Figure 9
Fragment velocity distribution versus spray angle Θ - charge B

The fragment recovery tests considered in this work were performed employing disposable plastic containers measuring approximately 52 in. in diameter and 59 in. in height, filled with approximately 1000 lbs of sawdust. After inserting the tested round in an inflatable rubber balloon and filling the balloon with air, the balloon was positioned in the sawdust in the middle of the plastic container. After detonating the round, the resulting fragments were recovered employing a combination of the magnetic (for separating fragments from the sawdust) and the vacuum (for separating sawdust from the fragments) recovery techniques. The mass distribution of the collected fragments was analyzed employing an electronic high precision balance gauge interfaced with a computer system capable of automatic counting of fragments as they were placed on the scale and weighed. Weighing of the fragments was performed employing the Ohaus Voyager Balance model V14130 gauge with the maximum capacity of 410 g and the precision of 0.001 g. A total of two sawdust recovery tests were performed, each of the tests resulting in successful recovery of approximately over 99.8% of the mass of the steel shell.

Figure 10 shows plots of CALE-MOTT analytic predictions of the cumulative number of fragments compared with the data from the fragment recovery tests. As shown in the figure, two analytic relationships had been considered: (i) the "shell-averaged" fragment size distribution (eq 14) and (ii) the "ring-segment-averaged" fragment size distribution (eq 17). As shown in the figure, the analytic prediction of equation 14 significantly disagrees with the experimental data, regardless of the value γ considered. The disagreement between the equation 14 predictions and the data is mostly because of the significant variance in fragment weights μ_j along the shell, ultimately resulting in over-predicting the "shell-averaged" fragment weight $\tilde{\mu}_0$ (eq 16). On the contrast, the agreement between the data and the γ=14 "ring-segment-averaged" fragment size distribution given by the equation 17 is quite good: $\sigma_{\gamma=14}(0.1944)$=-7.3%. Given relative simplicity of the model, the overall agreement between the analyses and the data is excellent.

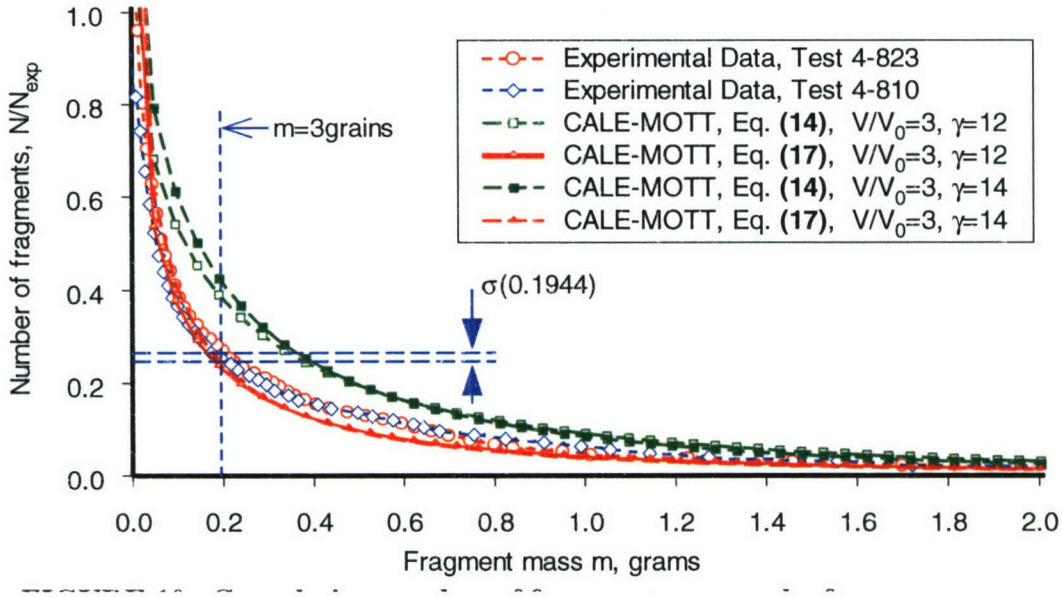

Figure 10
Cumulative number of fragments versus the fragment mass m - charge B

CONCLUSIONS

A technique for predicting performance of explosive fragmentation munitions presented in this work is based on integrating three-dimensional axisymmetric hydrocode analyses with analyses from a newly developed fragmentation computer code MOTT. The validation of the MOTT code fragmentation model was accomplished using the existing munition arena test data. After having established the crucial parameters of the model, a new explosive fragmentation munition was designed and optimized. Upon fabrication of the developed munition, the performance of the new charge was tested in a series of small-scale experiments including the flash radiography, the high-speed photography, and the sawdust fragment recovery. Considering relative simplicity of the model, the accuracy of the MOTT code predictions is rather remarkable.

REFERENCES

1. Tipton, R. E., "CALE Users Manual", Version 910201, Lawrence Livermore National Laboratory, 1991.

2. Tipton, R. E., "EOS Coefficients for the CALE Code for Some Materials", Lawrence Livermore National Laboratory, 1991.

3. Mott, N. F., F.R.S., "Fragmentation of Steel Cases", Proc. Roy. Soc., 189, pp. 300-308, 1947.

4. Mott, N. F. and Linfoot, E. H., "A theory of fragmentation", Ministry of Supply, A.C. 3348, January 1943.

5. Pearson, J., "A Fragmentation Model for Cylindrical Warheads", Technical Report NWC TP 7124, Naval Weapons Center, China Lake, California, December 1990.

DISTRIBUTION LIST

U.S. Army ARDEC
ATTN: AMSRD-AAR-EMK
AMSRD-AAR-GC
AMARD-AAR-AEE-W, E. Baker
V. Gold (5)
AMSRD-AAR-AEM-J, J. Hirlinger
G. Flemming
AMSRD-AAR-AEW-M(D), S. Liss
G. Moshier
AMSRD-AAR-AEM-D, G. Voorhis
Picatinny Arsenal, NJ 07806-5000

Defense Technical Information Center (DTIC)
ATTN: Accessions Division
8725 John J. Kingman Road, Ste 0944
Fort Belvoir, VA 22060-6218

Commander
Soldier and Biological/Chemical Command
ATTN: AMSSB-CII, Library
Aberdeen Proving Ground, MD 21010-5423

Director
U.S. Army Research Laboratory
ATTN: AMSRL-CI-LP, Technical Library
Bldg. 4600
Aberdeen Proving Ground, MD 21005-5066

Chief
Benet Weapons Laboratory, AETC
U.S. Army Research, Development and Engineering Command
Armament Research, Development and Engineering Center
ATTN: AMSRD-AAR-AEW
Watervliet, NY 12189-5000

Director
U.S. Army TRADOC Analysis Center-WSMR
ATTN: ATRC-WSS-R
White Sands Missile Range, NM 88002

Chemical Propulsion Information Agency
ATTN: Accessions
10630 Little Patuxent Parkway, Suite 202
Columbia, MD 21044-3204

GIDEP Operations Center
P.O. Box 8000
Corona, CA 91718-8000

Alliant Tech Systems
ATTN: C. Nelson
G. Holms
600 Second Street, NE
Hopkins, MN 55343